Optical and Quantum Electronics (2025) 57:78
https://doi.org/10.1007/s11082-024-07991-3

Design of compact 1×4 fully non-blocking silicon-photonic mode selective switch

Ho Duc Tam Linh[1,5] · Vuong Quang Phuoc[1] · Dang Thanh Chuong[1] · Vo Duy Phuc[2] · Dao Duy Thang[3] · Truong Cao Dung[4] · Nguyen Tan Hung[2]

Received: 7 August 2024 / Accepted: 10 December 2024

Abstract
We propose a novel 1×4 non-blocking four-mode selection switch on a silicon-on-insulator (SOI) substrate. It comprises one Y-Junction coupler, six Phase Shifters (PS), and three Multimode Interferences (MMI). While the Y-Junction is designed to divide modes at the input of the device, the MMIs direct signals from its inputs to suitable outputs by adjusting the value of the Phase Shifters. The outstanding feature is that the proposed switch allows the four input modes ($TE_0 - TE_1 - TE_2 - TE_3$) to be guided simultaneously or sequentially to the desired output without any discontinuation. Through BPM-3D beam propagation with the EIM effective index method, it is shown that the device is capable of smoothly switching concurrently or, in turn, the four modes mentioned above from any input to any output with insertion loss (IL) being smaller than 0.1 dB at the central wavelength 1.55 μm, and crosstalk (CT) being from −48 dB to −19 dB for the entire C band.

✉ Ho Duc Tam Linh
hdtlinh@hueuni.edu.vn

Vuong Quang Phuoc
vqphuoc@hueuni.edu.vn

Dang Thanh Chuong
dtchuong@hueuni.edu.vn

Vo Duy Phuc
vdphuc@dut.udn.vn

Dao Duy Thang
katsiusa@gmail.com

Truong Cao Dung
dungtc@ptit.edu.vn

Nguyen Tan Hung
hung.nguyen@ac.udn.vn

[1] University of Sciences, Hue University, Hue, Vietnam

[2] The University of Danang-University of Science and Technology, Danang, Vietnam

[3] Silicon Austria Labs, Villach, Austria

[4] Posts and Telecommunications Institute of Technology, Hanoi, Vietnam

[5] The University of Danang-Advanced Institute of Science and Technology, Danang, Vietnam

Published online: 26 December 2024

Keywords Mode selective switch · MMI · Y-Junction · MDM

1 Introduction

Optical communications and interconnects utilizing silicon photonics integrated circuits have enormous potential in realizing large-capacity information networks (Paniccia 2011; Zhao et al. 2015; Dai and Bowers 2014; Igarashi et al. 2016). This topic has been extensively studied thanks to many outstanding advantages, such as CMOS technology compatibility, high-scale integration, and high optical conversion efficiency. In recent years, alongside the well-employed wavelength division multiplexing (WDM), the emerging mode-division-multiplexing (MDM) has also been widely investigated as it can remarkably enhance the bandwidth even when only one wavelength is in use Chen et al. (2014); Luo et al. (2014); Wang et al. (2014); Qiu et al. (2013). Since data channels are independently carried on orthogonal eigenmodes of the same wavelength without inter-channel crosstalk, total transmission capacity could have multiple rises when MDM is in combination with WDM (Absil 2014; Engineering 2014; Mulugeta and Rasras 2015).

Despite much MDM research, this MDM technology still needs to overcome many challenges, including optically multimode signal switching for MDM communication and interconnect systems. This network functionality can be carried out through optical mode selective switching (MSS), which can direct arbitrary modes to the desired outputs without blocking. Here, a non-blocking mode switch is a mechanism that establishes a path from any mode at input to any output (Sharma 1999). Analogously to its WDM counterpart, wavelength selective switch (WSS), MSS is one of the key elements to realize optical space and mode switches or reconfigurable optical add-drop multiplexers (ROADMs) for MDM networks (Nguyen et al. 2020; Wang and Hao 2016; Mojaver et al. 2024). MSS has been extensively demonstrated, relying on various principles, structures, and materials. For multimode fibers (MMFs), MSS has been presented by using spatial light modulators (SLMs) (Cao et al. 2023; Labroille et al. 2014; Kumar et al. 2018; Labroille et al. 2014; Igarashi et al. 2014) or optical micro-electromechanical systems (MEMS) (Hayashi et al. 2015; Chan and Chan 2014; Zi et al. 2018; Huang et al. 2018) posterior to a mode demultiplexer. In general, these systems attain good performance, yet they are bulky, costly, and unable to integrate.

For integration supporting MSS devices, different waveguide structures such as multimode interferometer (MMI) (Priti and Liboiron-Ladouceur 2019; Priti et al. 2017), long-period waveguide gratings (Jin 2018), microring resonators (MRRs) (Jia et al. 2019), directional couplers (DCs) (Liu et al. 2022; Jiang and Rahman 2020), and Mach-Zehnder interferometers (MZIs) (Liu et al. 2021; Zhang et al. 2020) have also been used based on silicon-on-insulator (SOI), polymer or silica materials. One main drawback of these demonstrations so far was that they only supported two or three modes. This restricts their applications for larger-capacity MDM systems. In principle, one straightforward solution is to combine a passive mode demultiplexer with a non-blocking single-mode optical switch to increase the number of modes for MSS. However, this solution has a large footprint and high insertion loss, generally scaled up as the number of modes increases. It becomes even more challenging as a path-independent-insertion-loss (PILOSS) topology is required for the optical switch (Konoike et al. 2023; Chen et al. 2013; Liangjun et al. 2016; Cao et al. 2020; Yong Zhang et al. 2017). For example, a 1×4 mode demultiplexer, which is comprised of cascaded asymmetric Y-junctions, would have a length of up to 25000 μm

(Chen et al. 2013), while a 4×4 non-blocking PILOSS optical switch would need sixteen 2×2 Mach-Zehnder (MZ) switching elements, each has a footprint of approximately 250× 120 μ m^2 (Liangjun et al. 2016). As a result, a 1×4 MSS based on the above combination would have an enormous footprint, which is impractical for photonic integrated circuit applications.

This paper proposes a compact design for MSS that can conduct more information channels in the MDM system. It allows four modes of TE_i (i = 0, 1, 2, 3) to be switched to the designed outputs synchronously and with no restriction, which we could describe as a fully non-blocking MSS. More importantly, the proposed MSS exhibits a PILOSS topology with low insertion loss and crosstalk when only three cascaded MMIs are used. This is far more advantageous than the device suggested in Tang et al. (2017), where a minimum number of cascaded MMI stages equivalent to the number of modes is required. The suggested device's platform extends our previous design on an arbitrary four-mode converter mentioned in Linh et al. (2020). Here, three MMIs of two types are utilized, and each type operates with a dedicated switching characteristic to carry out the functionalities of the MSS simultaneously. By setting the appropriate value for the Phase Shifters before the MMIs, four input modes are routed concurrently to the desired destinations with no conflict. Our work uses numerical simulations based on the dimensional-beam propagation method (BPM) with the effective index method (EIM) to design and optimize the device. The simulation results clarify that the performance of switched signals at the output is consistently above 98% at a central wavelength of 1.55 μm, and the crosstalk is always less than −19 dB in the entire C band.

2 Structure design

2.1 General description

This section will give a general description of the proposed four-mode MSS, plotted in Fig. 1a. It consists of a 1×4 Y-Junction coupler and three 4×4 MMI couplers; each MMI is accompanied by two Phase Shifters located at two input ports on the left side. For the 1×4 Y-junction coupler, while being converted into fundamental modes TE_0, signals of TE_0, TE_1, TE_2, and TE_3 modes are equally split into two of the four output ports in a fashion based on the mode order at the input. Among the three 4×4 MMI couplers, the first two MMIs are of one type, while the third one is of another type; both possess different lengths for dedicated switching characteristics.

The first two MMIs produce complete switching variations for a group of two signals of any two modes among four modes to be co-resident at a pair of output ports of the second MMI. The third MMI, in turn, combines and routes these signals to the desired outputs of the MSS. By setting suitable values for the Phase Shifters, the input signals at different modes can be selectively switched to the output ports of the device without blocking. This design allows four modes TE_i (i = 0, 1, 2, 3) to be transmitted simultaneously at the same input to four output ports O_j (j = 1, 2, 3, 4) in any order without contention between the signals. In addition, if the signals are transmitted sequentially, the TE_i signal that arrives first at the input port will have the highest priority in selecting one of the four desired output ports. The TE_i signal that arrives next at the input port will have the second priority of choosing the remaining output ports. Thus, the third TE_i signal that is transmitted immediately after will have two choices to

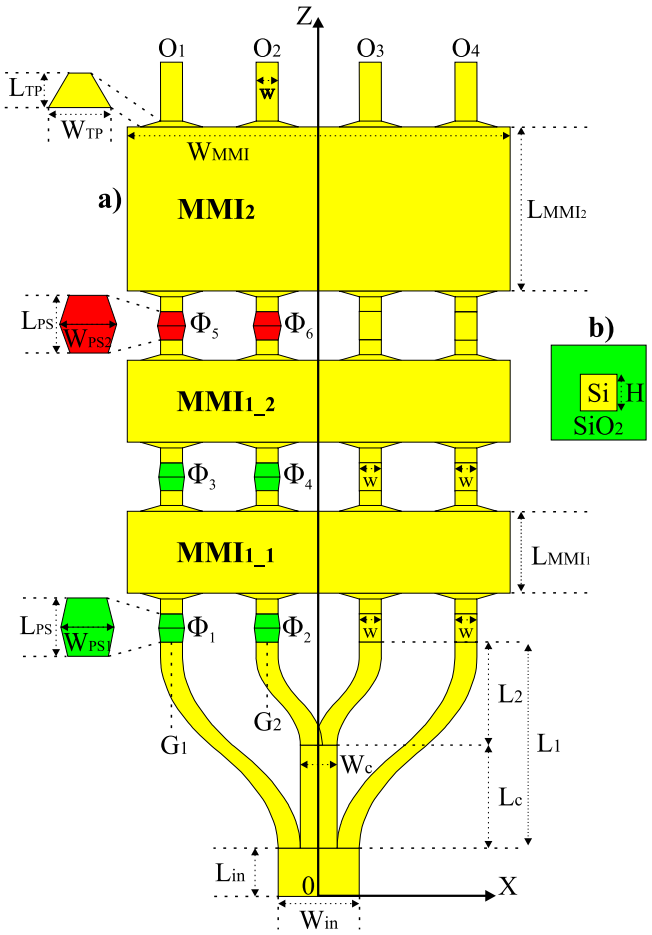

Fig. 1 Structure of proposed mode-selective switch

select one of the two remaining ports, meaning that the fourth port not occupied by the previous three signals will be reserved for the fourth TE_i signal. The operating principle, together with the design and optimization of the Y-Junction coupler and the MMI couplers, will be presented in the following sections.

The cross-section of the input waveguide is shown in Fig. 1b with the height of the channel structure H = 0.22 μm. The proposed structure has a Si core layer placed between two SiO_2 layers. Refractive indices of the core, lower, and upper cladding layers at the wavelength 1.55 μm are set at 3.47, 1.44, and 1.44, respectively. This paper uses numerical simulation based on the beam propagation method (BPM) with the effective index method (EIM) to design, optimize, and evaluate the device's performance.

2.2 1x4 Y-junction coupler

Figure 2 shows the concept of the 1×4 Y-Junction coupler as four different order modes are applied to the input waveguide. The 1×4 Y-Junction coupler is designed to convert higher-order modes into fundamental modes TE_0. At the same time, it divides four input signals of modes TE_0, TE_1, TE_2, and TE_3 into two groups, i.e. (TE_0 and TE_3) and (TE_1 and TE_2), which are co-resident at two of the four output waveguides of the coupler. While the TE_0 and TE_3 signals are equally split into two inner waveguides (arms 2 and 3), the TE_1 and TE_2 signals are equally split into two outer waveguides (arms 1 and 4), as shown in Fig. 2a and b, respectively. Note here that the signals split into the arms are in phase for even-order modes TE_0 and TE_2 and out of phase for odd-order modes TE_1 and TE_3.

An input waveguide with a width of W_{in} and a length of L_{in} is placed at the input of the 1×4 Y-Junction coupler (Fig. 1a). The input waveguide is split up into three narrower waveguides. The central one, having a width of W_c and a length of L_c, guides two modes, TE_0 and TE_1. It is then separated into two other waveguides. As a result, four arms are at the output of the coupler; all have the same width of w and support only TE_0 mode. To determine the width of the waveguides, in Fig. 3, effective refractive indices are studied as a function of the width of the waveguide for different modes. Here, the width of the input waveguide of the Y-Junction W_{in} is 1.2 μm, which is wide enough to allow synchronous transmissions of four modes: TE_0, TE_1, TE_2 and TE_3. The length of the input waveguide is set at 30 μm. We choose the width of waveguides w and W_c based on suitable mode conversion compatibility and high optical conversion efficiency. For example, when a TE_3 mode signal is transmitted into the W_{in} waveguide, this TE_3 mode signal will be converted to a TE_1 mode signal when sent through the central waveguide W_c. Through simulation, we determine that at $W_c = 0.6$ μm, the mode conversion efficiency reaches its highest value. Similarly, we achieve the highest conversion efficiency at $w = 0.3$ μm when converting the TE_1 mode in the W_c waveguide into two TE_0 modes in the output arms. The four arms at the outputs of the coupler are S-bent waveguides featured by vertical lengths and horizontal widths, which are L_1 and G_1 for the outer arms and L_2 and G_2

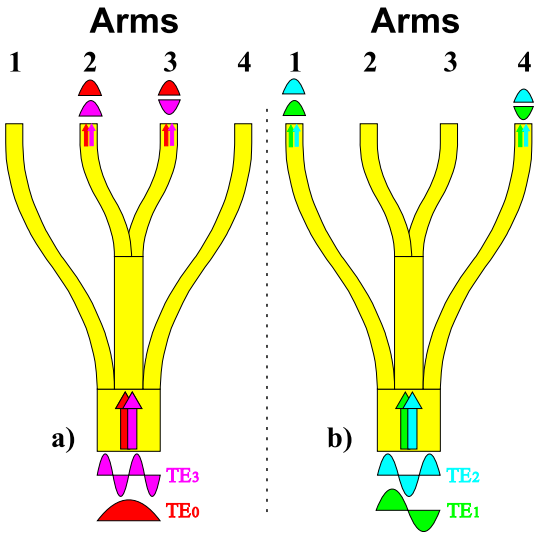

Fig. 2 Mode demultiplexing of 1×4 Y-junction coupler for input modes TE_0 and TE_3 (**a**), and input modes TE_1 and TE_2 (**b**)

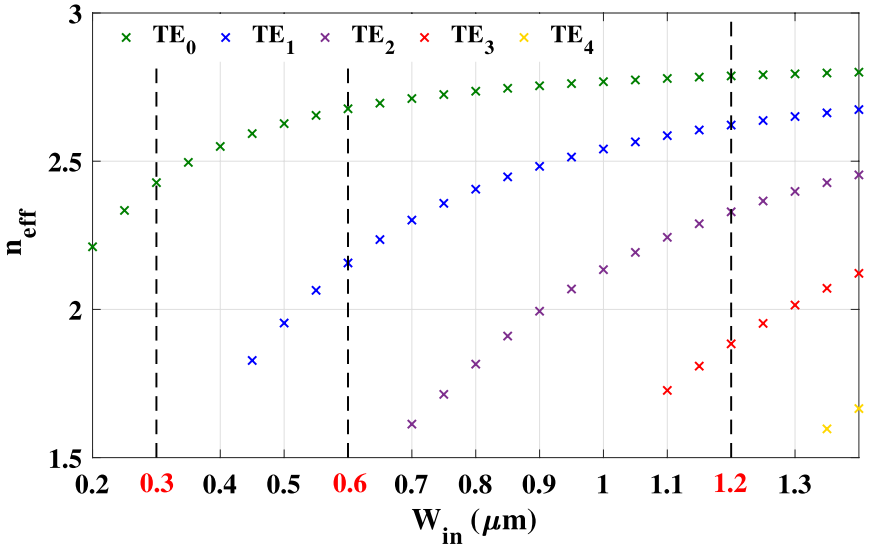

Fig. 3 Support modes according to waveguide width W_{in}

for the inner arms. The vertical lengths of the outer and inner arms are designed so that $L_1 = L_2 + L_c$ to ensure all four arms have the same level before the first 4×4 MMI.

The input light field of the Y-Junction coupler at position z = 0 in the x-coordinate width direction is $Y_m(x, 0)$. This field transfers through the waveguide of length L and has the following form:

$$Y_m(x, L) = Y_m(x, 0)e^{j\beta_m L} \tag{1}$$

Where β_m is the propagation constant at the mode $m - th$ (m = 0, 1, 2, 3), the mode field $Y_m(x, L)$ is divided into sub-fields at the Y-Junction coupler's arms $a - th$ (a = 1, 2, 3, 4).

$$Y_m(x, L) = \sum_{a=1}^{4} \delta_{am} y_{am}(x) \tag{2}$$

δ_{am} and y_{am} are the field excitation coefficients and mode field distribution of $m - th$ mode at the $a - th$ output arm, where δ_{am} is evaluated by calculating the overlap integral formula.

$$\delta_{am} = \frac{\int Y_m(x, L) y_{am}(x)\, dx}{\sqrt{\int y_{am}^2(x)\, dx}} \tag{3}$$

We estimate the power excitation coefficients $c_{am} = |\delta_{am}|^2$ at the output arms of the Y-Junction coupler for each mode $m - th$ based on the 3D-BPM simulation. The results in the Fig. 4 show the relationship between the c_{am} coefficients and the length L_2 of the bent waveguides of the Y-Junction coupler. With the L_2 value greater than 7 μm, the conversion efficiency is highest from the higher-order modes to the fundamental modes in the arms. In this design, we set $L_1 = 58$ μm, $L_2 = 8$ μm and $L_c = 50$ μm.

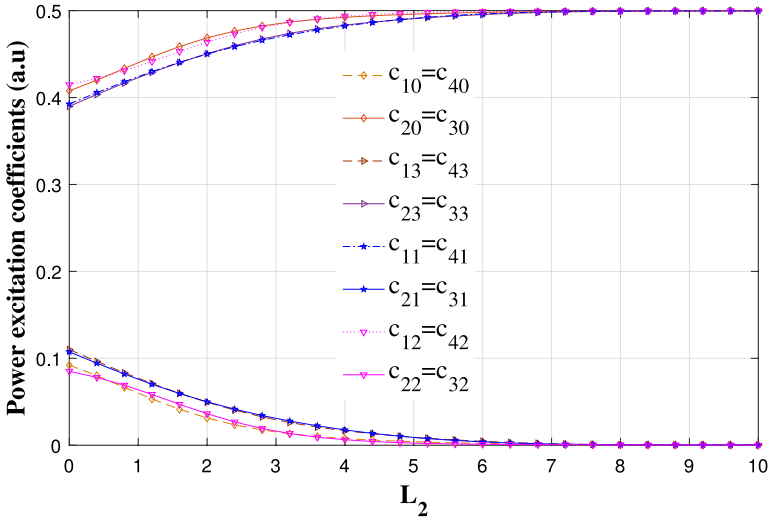

Fig. 4 The arm's length of L_2 according to c_{am} power excitation coefficients

2.3 Multimode interference couplers

The MMI couplers are rectangular waveguides with the same width as the W_{MMI}, operating according to self-imaging phenomena. As presented in the general description of the device, the first two 4×4 MMIs (MMI_{1_1}, MMI_{1_2}) have the same design with a length L_{MMI1}, and the third MMI has a different length L_{MMI2}.

The length of the rectangle is chosen, following the general interference mechanism (Soldano 1995), it means $L_{MMI1} = 3L_\pi/4$, $L_{MMI2} = 3L_\pi/2$ with L_π as the beat length of the two lowest-order modes in the MMI region and it is given by:

$$L_\pi = \frac{4n_{eff}W_{eff}^2}{3\lambda_0} \tag{4}$$

with

$$W_{eff} = W_{MMI} + \frac{\lambda_0}{\pi}\left(n_{eff}^2 + n_c^2\right)^{-\frac{1}{2}} \tag{5}$$

Where W_{eff} is the effective width of the MMI waveguide, free-space wavelength λ_0, effective refractive index n_{eff}, and effective cladding refractive index n_c, the access waveguides are numbered from left to right 1, 2, 3, and 4 for the input and output waveguides of MMI. These input and output waveguides are set symmetrically to each other concerning the central axis of the device at positions: $G_1 = \pm 2.7$ μm and $G_2 = \pm 0.8$ μm. According to calculation, the length of $L_{MMI1} = 88$ μm, $L_{MMI2} = 176.2$ μm and the same width of $W_{MMI} = 6.8$ μm.

In addition, the optical phases of the fields in a N×N MMI coupler are given by Soldano (1995).

$$\varphi_{rs} = \frac{\pi}{4N}(s - r)(2N - s + r) + \pi \tag{6}$$

for r + s even
and

$$\varphi_{rs} = \frac{\pi}{4N}(s + r - 1)(2N - s - r + 1) \tag{7}$$

for r + s odd

Where N is the number of input and output ports of the MMI coupler, r = 1, 2, 3, ...N is the numbering of input access waveguides (bottom-up), s = 1, 2, 3, ...N is the numbering of output access waveguides (top-down), and φ_{rs} is the phase difference between port s and port r.

To facilitate the description process, we numbered four input and output ports of an MMI from left to right: 1, 2, 3, and 4. There are four mode-switching scenarios when two TE_0 signals are simultaneously transmitted to the symmetric ports of the MMI_1 (Fig. 5). If the two signals with the same phase and amplitude are applied to input ports 1 and 4 (or input ports 2 and 3), they will exit the MMI_1 at output ports 1 and 4 (or output ports 2 and 3, respectively). However, if the input signals applied to input ports 1 and 4 (or ports 2 and 3) are out of phase with each other, the signals will be directed to output ports 2 and 3 (or output ports 1 and 4, respectively).

In MMI_2, the signals emitted at two input ports, 2 and 3 (or input ports 1 and 4), with a phase difference of 90 degrees, will produce a single signal with a double amplitude at the output port (Fig. 6). In the case of inputting signals at ports 2 and 3, if the signal's phase at port 2 is 90 degrees faster than that of one at port 3, the output signal will appear at port 3. In contrast, the signal will appear at the output port number 2 if the signal phase at port 3 is faster than 90 degrees. If two signals are transmitted at ports 1 and 4, a composite signal is selected at output port number 1 or 4 with the same property as the case of signals on ports 2 and 3.

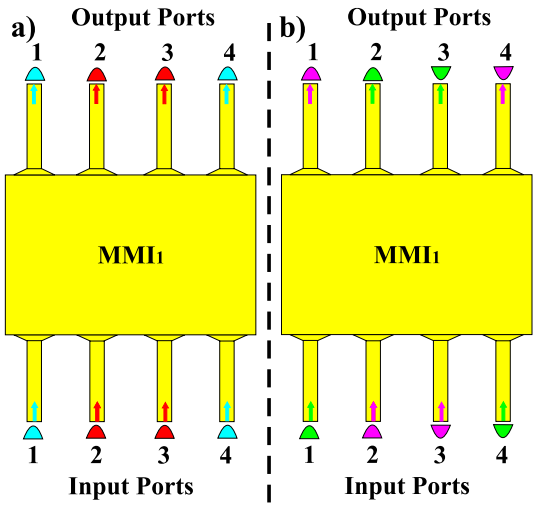

Fig. 5 Principle of operation of MMI_1 couplers. **a** two signals in phase; **b** two signals out of phase

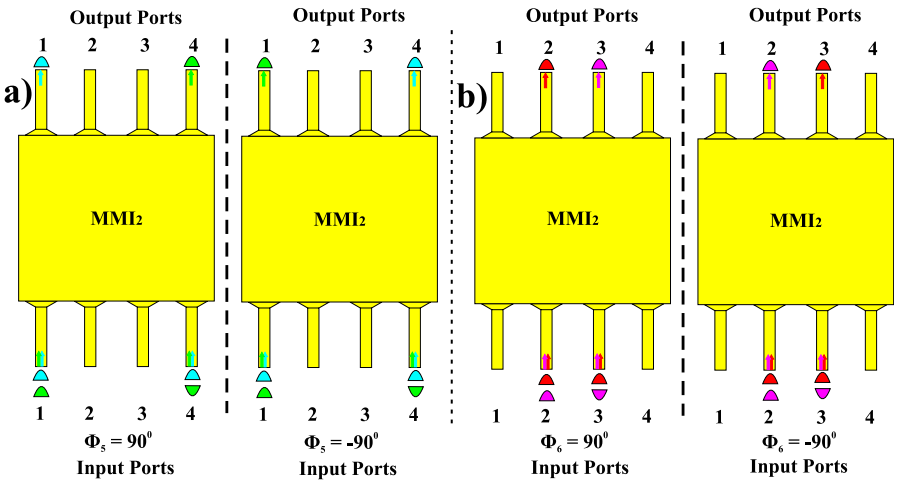

Fig. 6 Principle of operation of MMI_2 couplers. **a** Synthesize two signals at two external ports; **b** Synthesize two signals at two internal ports

2.4 Phase shifter

The device uses three types of Phase Shifters corresponding to their values: −90, 90, and 180 degrees. With the fixed length $L_{ps} = 10\ \mu m$, the phase change is investigated as a function of the center width W_{ps} of the Phase Shifter, as illustrated in Fig. 7. To obtain −90 degrees, 90 degrees, and 180 degrees phase shift, W_{ps} is set at 0.33 μm, 0.38 μm, and 0.35 μm, respectively. Although tunable Phase Shifters are utilized in practice, fixed ones are used in this paper to simulate the concept of the proposed MSS. The six Phase Shifters must be set to the appropriate value to guide signals correctly. With four

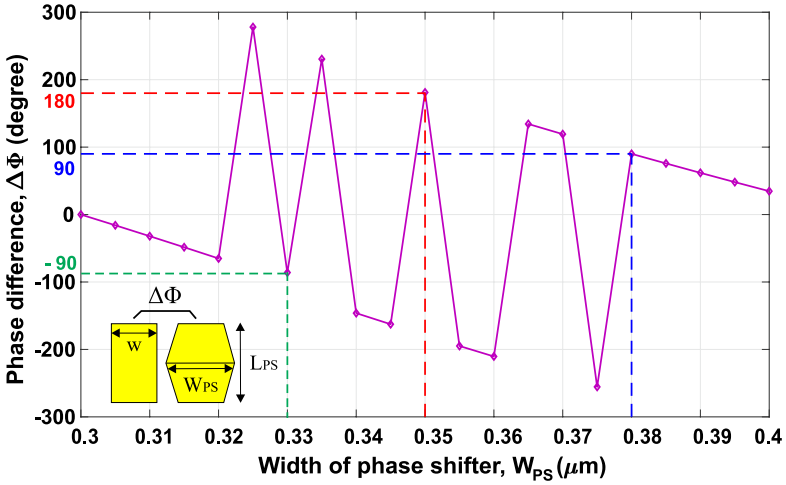

Fig. 7 Phase shifting value as functions of the central width W_{ps} Phase Shifter

modes at the single input and four output ports, twenty-four general cases are described in Table 1.

In Table 1, the priority order is from TE_0 to TE_3. This means that if the input mode TE_0 chooses the output O_1, the TE_1 input mode only has the remaining three options, which correspond to the first six cases in Table 1. Assuming that the TE_1 mode signal selects output O_3, there are only two output ports (O_2, O_4) for TE_2 and TE_3 to adopt (respectively, switching cases 3 and 4). Supposing the TE_2 signal picks out the O_2 output, the TE_3 mode signal must be guided to output port O_4 (case 3). Otherwise, if the TE_2 mode signal selects the O_4 output, the remaining port O_2 must be for the TE_3 signal (case 4).

3 Performance evaluation and discussion

The two methods of BPM-3D and EIM are used to achieve precise and detailed illustrations for correct mode switching of the devices. The image field distribution of modes from the inputs to outputs is shown in Fig. 8. We show two cases of transmitting signals from TE_0 to TE_3 (cases 1 and 7) corresponding to the phase values ($\Phi_1, \Phi_2, \Phi_3, \Phi_4, \Phi_5, \Phi_6$)

Table 1 Values of phase shifters

Case	$TE_i \rightarrow O_j$	Phase shifters ($\Phi_1, \Phi_2, \Phi_3, \Phi_4, \Phi_5, \Phi_6$)
1	$TE_{(0,1,2,3)} \rightarrow O_{(1,2,3,4)}$	(0^0, 0^0, 180^0, 180^0, -90^0, 90^0)
2	$TE_{(0,1,2,3)} \rightarrow O_{(1,2,4,3)}$	(0^0, 0^0, 0^0, 180^0, -90^0, 90^0)
3	$TE_{(0,1,2,3)} \rightarrow O_{(1,3,2,4)}$	(0^0, 0^0, 180^0, 180^0, -90^0, -90^0)
4	$TE_{(0,1,2,3)} \rightarrow O_{(1,3,4,2)}$	(0^0, 0^0, 0^0, 180^0, -90^0, -90^0)
5	$TE_{(0,1,2,3)} \rightarrow O_{(1,4,2,3)}$	(180^0, 0^0, 0^0, 180^0, -90^0, 90^0)
6	$TE_{(0,1,2,3)} \rightarrow O_{(1,4,3,2)}$	(180^0, 0^0, 0^0, 180^0, -90^0, -90^0)
7	$TE_{(1,0,2,3)} \rightarrow O_{(1,2,3,4)}$	(0^0, 0^0, 180^0, 0^0, -90^0, 90^0)
8	$TE_{(1,0,2,3)} \rightarrow O_{(1,2,4,3)}$	(0^0, 0^0, 0^0, 0^0, -90^0, 90^0)
9	$TE_{(1,0,2,3)} \rightarrow O_{(1,3,2,4)}$	(0^0, 0^0, 180^0, 0^0, -90^0, -90^0)
10	$TE_{(1,0,2,3)} \rightarrow O_{(1,3,4,2)}$	(0^0, 0^0, 0^0, 0^0, -90^0, -90^0)
11	$TE_{(1,0,2,3)} \rightarrow O_{(1,4,2,3)}$	(0^0, 180^0, 180^0, 0^0, -90^0, -90^0)
12	$TE_{(1,0,2,3)} \rightarrow O_{(1,4,3,2)}$	(0^0, 180^0, 180^0, 0^0, -90^0, 90^0)
13	$TE_{(2,0,1,3)} \rightarrow O_{(1,2,3,4)}$	(0^0, 180^0, 0^0, 180^0, 90^0, -90^0)
14	$TE_{(2,0,1,3)} \rightarrow O_{(1,2,4,3)}$	(0^0, 180^0, 0^0, 0^0, 90^0, -90^0)
15	$TE_{(2,0,1,3)} \rightarrow O_{(1,3,2,4)}$	(0^0, 180^0, 0^0, 180^0, 90^0, 90^0)
16	$TE_{(2,0,1,3)} \rightarrow O_{(1,3,4,2)}$	(0^0, 180^0, 0^0, 0^0, 90^0, 90^0)
17	$TE_{(2,0,1,3)} \rightarrow O_{(1,4,2,3)}$	(0^0, 0^0, 0^0, 180^0, 90^0, 90^0)
18	$TE_{(2,0,1,3)} \rightarrow O_{(1,4,3,2)}$	(0^0, 0^0, 0^0, 180^0, 90^0, -90^0)
19	$TE_{(3,0,1,2)} \rightarrow O_{(1,2,3,4)}$	(180^0, 0^0, 180^0, 0^0, 90^0, 90^0)
20	$TE_{(3,0,1,2)} \rightarrow O_{(1,2,4,3)}$	(0^0, 0^0, 180^0, 0^0, 90^0, 90^0)
21	$TE_{(3,0,1,2)} \rightarrow O_{(1,3,2,4)}$	(180^0, 0^0, 180^0, 0^0, 90^0, -90^0)
22	$TE_{(3,0,1,2)} \rightarrow O_{(1,3,4,2)}$	(0^0, 0^0, 180^0, 0^0, 90^0, -90^0)
23	$TE_{(3,0,1,2)} \rightarrow O_{(1,4,2,3)}$	(0^0, 0^0, 180^0, 180^0, 90^0, 90^0)
24	$TE_{(3,0,1,2)} \rightarrow O_{(1,4,3,2)}$	(0^0, 0^0, 180^0, 180^0, 90^0, -90^0)

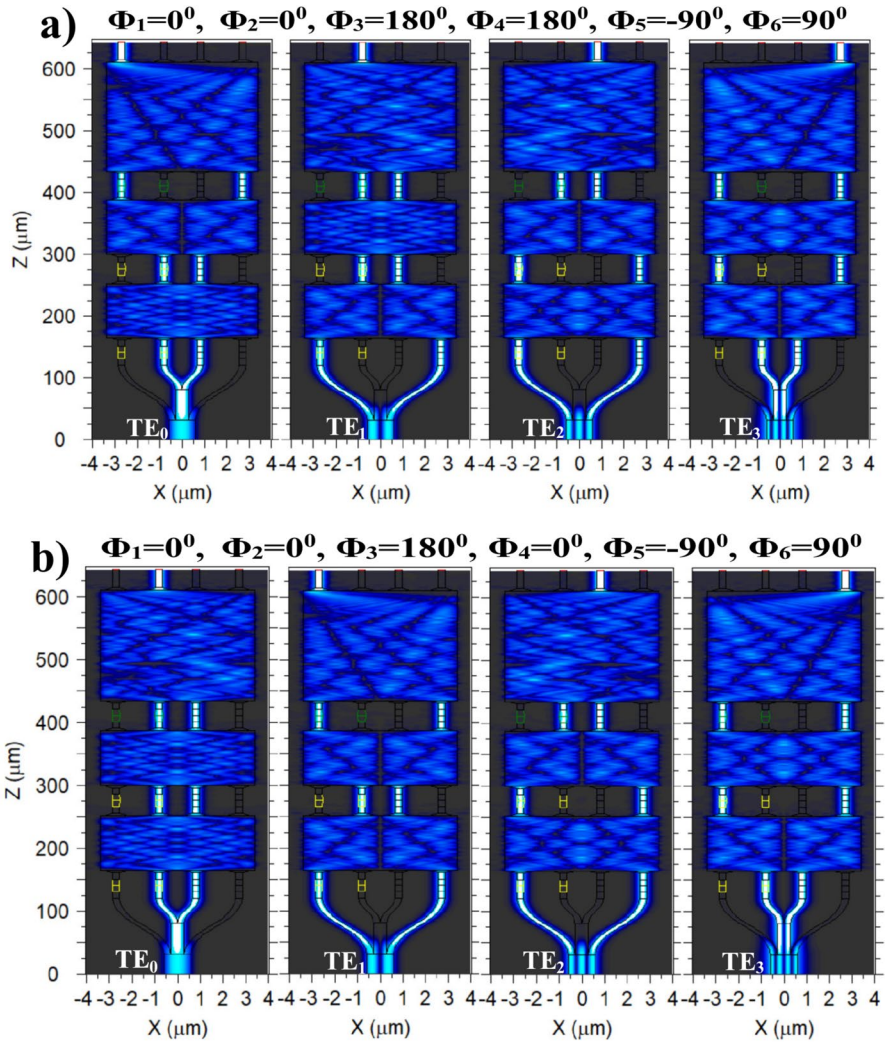

Fig. 8 The transverse electric field distribution of mode TE_i (i = 0, 1, 2, 3) to O_j output ports (j = 1, 2, 3, 4). **a** Case 1: $TE_{(0,1,2,3)} \rightarrow O_{(1,2,3,4)}$; **b** Case 7: $TE_{(1,0,2,3)} \rightarrow O_{(1,2,3,4)}$

shown in Table 1; it can seen that the input modes are routed to the desired output ports as described in theory. In addition, the outward optical power loss mainly occurs at the MMIs, not at the Y-Junction coupler. To evaluate the optical performance of the proposed device more thoroughly, we use two parameters, insertion loss (IL) and crosstalk (CT), and analyze them as functions of wavelength. Formulas of the two parameters are given as follows:

$$InsertionLoss(dB) = 10\log_{10}\left(\frac{P_{receive-desirable}}{P_{in}}\right) \tag{8}$$

$$Crosstalk(dB) = 10\log_{10}\left(\frac{\sum P_{receive-unwanted}}{P_{receive-desirable}}\right) \quad (9)$$

Where $P_{receive-desirable}$ is the received power at the desired output, P_{in} is the power of the input signal, and $P_{receive-unwanted}$ is the unwanted power at the remaining outputs. Based on the above formulas, the larger the IL and the lower the CT, the better the performance of the device is.

The simulation results are presented in Figs. 9, 10, 11, and 12, at the survey wavelength of 1.55 μm, the insertion loss is always less than 0.1 dB, and this value is always smaller than 3.6 dB in the entire band C (from 1.53 μm to 1.565 μm). Besides the high optical conversion power ratio, the crosstalk is also very low, always in the range of −48 dB to −19 dB in all 24 switching cases. Especially in all survey cases, insertion loss and crosstalk values are almost symmetrical through peak values at a wavelength of 1.55 μm. So, the graph is almost like a parabola shape. In addition, due to the geometrical symmetry between modes and between the placements of the input and output ports, the graph lines show that the IL or CT values at port pairs (O_1; O_4) and (O_2; O_3) almost overlap. Table 2 summarizes the function comparisons with published mode-selection switches. We want to distinguish further that partial non-blocking switching is the ability to switch the signals to all output ports. However, the signals are switched to the output ports at fixed positions with an initial control setting. Any change in the control setting will change the order of all signal channels at all output ports. On the contrary, a fully non-blocking is the ability to reconfigure without affecting the operation of other channels. With this comparison, the device structure in this paper has advantages in terms of the number of supported modes and fully non-blocking operation.

Finally, we investigated the effect of the gap G between the waveguides of the Y-Junction coupler on the mode conversion efficiency at the output of the arms. In this case, we transmitted the TE_1 and TE_3 mode signals into the input ports of the Y-Junction

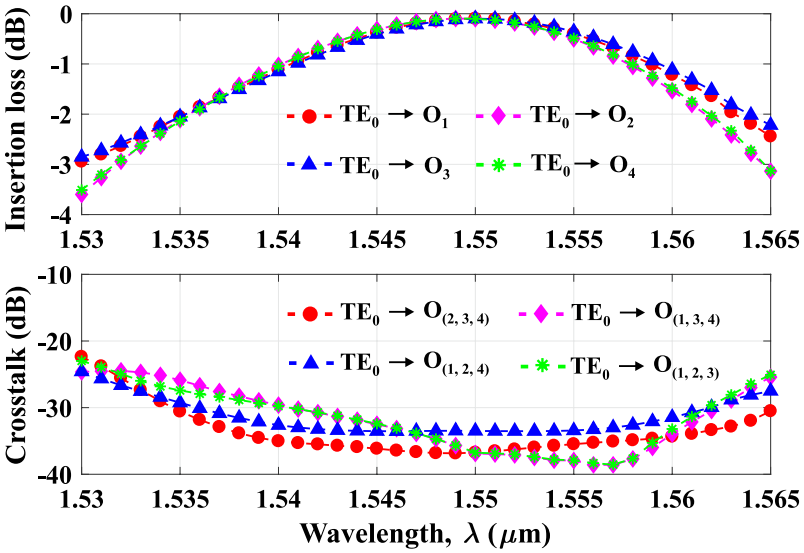

Fig. 9 Insertion loss and crosstalk for input signal TE_0 as a function of wavelength

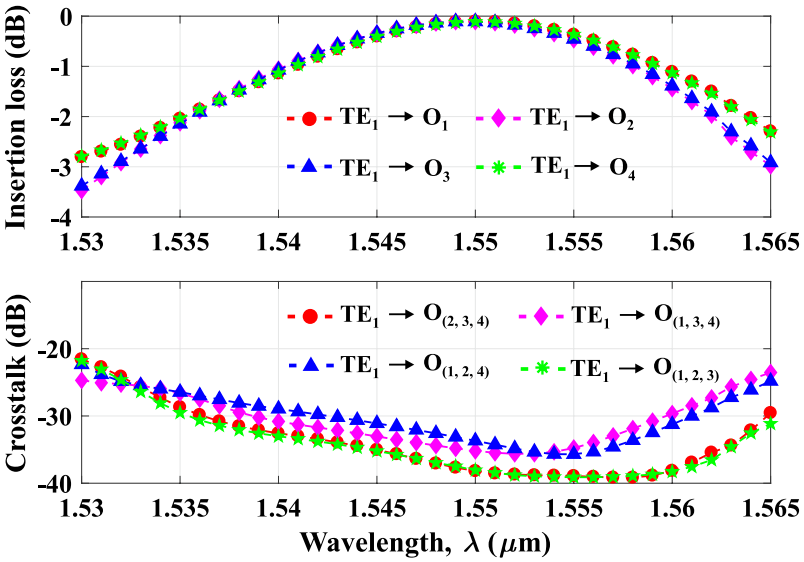

Fig. 10 Insertion loss and crosstalk for input signal TE_1 as a function of wavelength

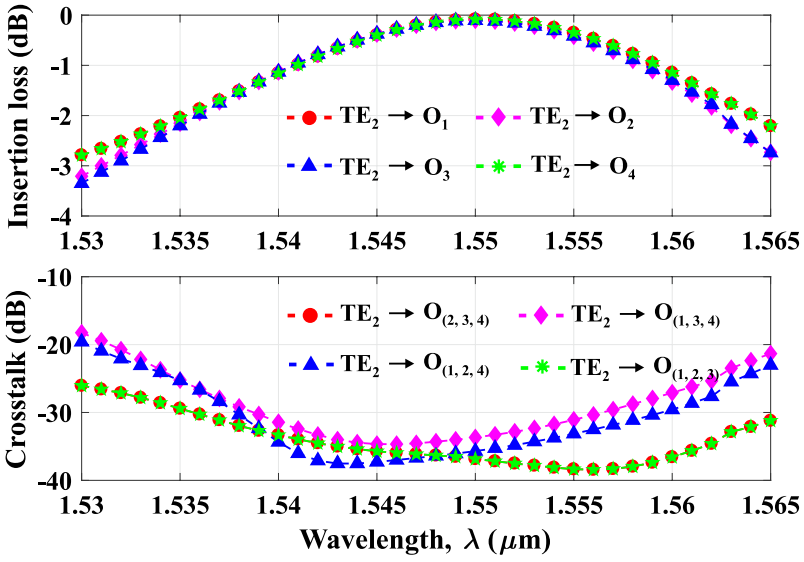

Fig. 11 Insertion loss and crosstalk for input signal TE_2 as a function of wavelength

coupler, respectively, and measured the power at the arms. The results showed that if the gap G was below 80 *nm*, the mode conversion efficiency at the output ports was not significantly affected. However, when the gap increased to $G = 120$ *nm*, the conversion efficiency decreased by approximately 5% of the power at each port and by approximately

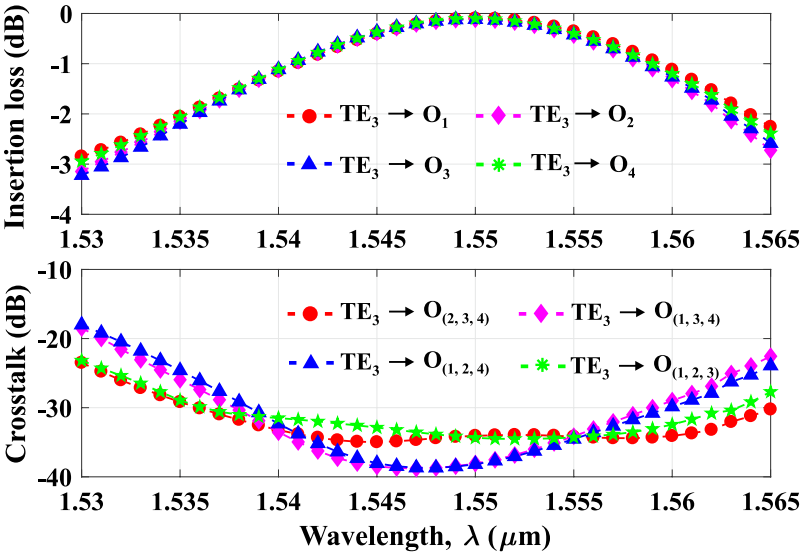

Fig. 12 Insertion loss and crosstalk for input signal TE_3 as a function of wavelength

Table 2 Compare functions with the published papers

Number of modes	Functions		
	Blocking	Partly non-blocking	Fully non-blocking
2		[42]	
2		[44]	
2		[46]	
2		[47]	
2		[50]	
3	[41]		
3	[25]		
3	[43]		
3	[45]		
3		[39]	
3		[48]	
4	[40]		
4	[49]		
4			This work

10% if the gap $G = 200\ nm$ (Fig. 13). The effect of the gap of the Y-Junction on the input modes TE_0 and TE_2 was similar to that of the input modes TE_1 and TE_3.

This gap affects the optical signal conversion performance of the entire device structure. Figure 14 shows the insertion loss and crosstalk of the signal at 1.55 μm wavelength when increasing the gap G from 0 to 200 nm. At the gap $G = 200\ nm$, the

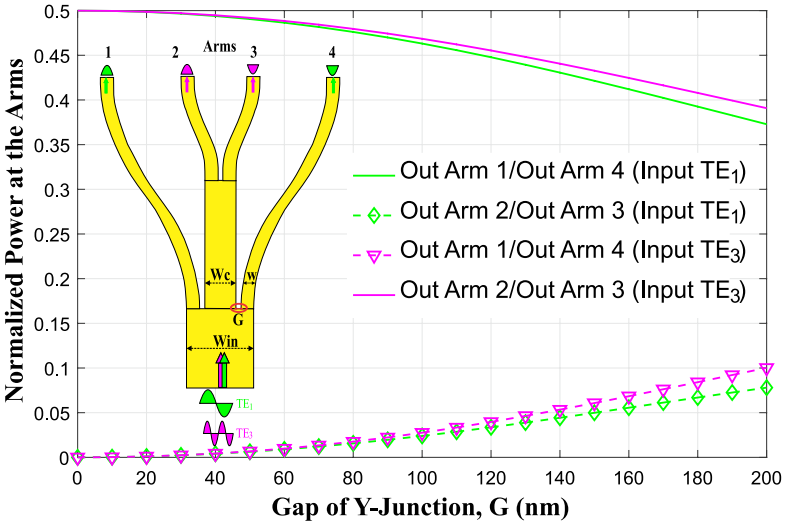

Fig. 13 The effect of gap G on the performance of the Y-Junction coupler

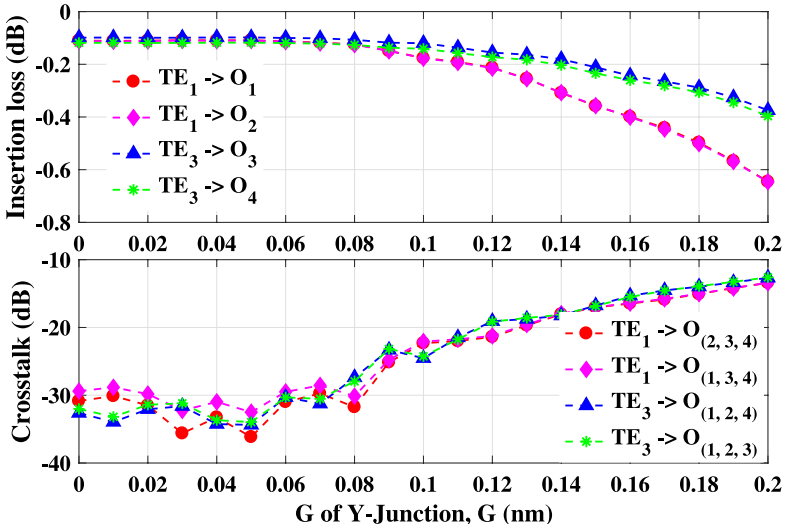

Fig. 14 Insertion loss and crosstalk for input signal TE_1 and TE_3 as a function of G

insertion loss of the TE_1 signal at the O_1 (or O_2) output ports is about 0.65 dB (approximately 86%), and the TE_3 signal at the O_3 (or O_4) output ports is about 0.4 dB (approximately 91%). Meanwhile, the crosstalk also decreases rapidly to −15 dB. These results show that the proposed device still ensures good optical performance in the actual fabrication conditions of the Y-Junction structure.

4 Conclusions

The paper presents a new full-function and non-blocking 1×4 mode-selective switch structure. Composed of only three cascaded MMI, the device supports up to four modes (TE_0, TE_1, TE_2, TE_3) to be guided accurately to the desired destination among the four outputs without disruption. The simulation results show superior optical performance with high mode selective switching efficiency at the entire C-band. Moreover, the crosstalk effect is also petite as this value is always in the ideal range from −48 dB to −19 dB. With such outstanding features, this device could be an essential component in the future of the reconfigurable MDM network.

Acknowledgements This research was supported by the Fund for Science and Technology Development of Hue University under project number DHH2024-01-216. The work of Vuong Quang Phuoc was funded by the Domestic Master/PhD Scholarship Programme of Vingroup Innovation Foundation (VINIF), code VINIF.2022.TS096.

References

Absil, P.P., et al.: "Advances in silicon photonics WDM devices,'' Next-Generation Opt. Netw. Data Centers Short-Reach Links **9010**, 90100J1–90100J7 (2014)

Bachmann, M., Besse, P.A., Melchior, H.: General self-imaging properties in NxN multimode interference couplers including phase relations. Appl. Opt. **33**(18), 3905–3911 (1994)

Cao, X., Zheng, S., Zhou, N., Zhang, J., Wang, J.: On-chip multi-dimensional 1 × 4 selective switch with simultaneous mode-polarization-wavelength-division multiplexing. IEEE J. Quantum Electron. **56**, 11–8 (2020)

Cao, H., Čižmár, T., Turtaev, S., Tyc, T., Rotter, S.: Controlling light propagation in multimode fibers for imaging, spectroscopy, and beyond. Adv. Opt. Photon. **15**, 524–612 (2023)

Chan, W.Y., Chan, H.P.: Reconfigurable two-mode mux/demux device. Opt. Express **22**, 9282–9290 (2014)

Chen, C. P., Driscoll, J., Souhan, B., Grote, R., Zhu, X., Osgood, R. M., Bergman, K.: "Experimental Demonstration of Spatial Scaling for High-Throughput Transmission Through A Si Mode-Division-Multiplexing Waveguide," in Advanced Photonics for Communications, Opt. Soc. America, 1–3 (2014)

Chen, W., Wang, P., Yang, J.: Mode multi/demultiplexer based on cascaded asymmetric Y-junctions. Opt. Express **21**, 25113–25119 (2013)

Dai, D., Bowers, J.E..: Silicon-based on-chip multiplexing technologies and devices for Peta-bit optical interconnects. Nanophoton. **3**(4–5), 283–311 (2014)

Ding, Y., Yin, Y., Guan, B., Zhiyuan, X., Yin, X., Yuanda, W., Sun, X., Zhang, D.: Mode-selective switch on silica-based PLC platform. Optic. Commun. **546**, 129757–129764 (2023)

Engineering, I.: "Mode division multiplexing network a deployment scenario in metro area network," 2154–2159, (2014)

Hayashi, H., Okamoto, A., Maeda, T., Shiba, T., Ogawa, K., Tomita, A., Takahata, T., Shinada, S., Goto, Y., Wada, N.: Mode-selective switch for ROADM using volume holograms and spatial light modulator. Proc. SPIE, Next-Generation Optical Communication: Components, Sub-Systems, and Systems IX, 1130905–1130908 (2020)

Hayashi, M., Diamantopoulous, N.P., Yoshida, Y., Maruta, A., Kitayama, K.: "Novel mode-selective packet switching,''. Photonic Switch., no. Topic **3**, 306–308 (2015)

Huang, Q., Chiang, K.S., Jin, W.: Thermo-optically controlled vertical waveguide directional couplers for mode-selective switching. IEEE Photonics J. **10**(6), 1–14 (2018)

Igarashi, K., Souma, D., Tsuritani, T., Morita, I.: Performance evaluation of selective mode conversion based on phase plates for a 10-mode fiber. Opt. Express **22**, 20881–20893 (2014)

Igarashi, K., Soma, D., Wakayama, Y., Takeshima, K., Kawaguchi, Y., Yoshikane, N., Tsuritani, T., Morita, I., Suzuki, M.: Ultra-dense spatial-division-multiplexed optical fiber transmission over 6-mode 19-core fibers. Opt. Express **24**, 10213–10231 (2016)

Jia, H., Xin, F., Zhou, T., Zhang, L., Yang, S., Yang, L.: Mode-selective modulation by silicon microring resonators and mode multiplexers for on-chip optical interconnect. Opt. Express **27**, 2915–2925 (2019)

Jiang, W., Rahman, B.M.A.: Compact and nonvolatile mode-selective switch with nano-heater. IEEE J. Sel. Top. Quantum Electron. **26**(5), 1–10 (2020)

Jiang, W., Miao, J., Li, T.: Silicon mode-selective switch via horizontal metal-oxide-semiconductor capacitor incorporated with ENZ-ITO. Sci. Rep. **9**, 17777, 1–12 (2019)
Jin, W.: Three-dimensional long-period waveguide gratings for mode-division-multiplexing applications. Opt. Express **26**(12), 15289–15299 (2018)
Konoike, R., Suzuki, K., Ikeda, K.: Path-independent insertion loss 8 × 8 silicon photonics switch with nanosecond-order switching time. J. Lightwave Technol. **41**(3), 865–870 (2023)
Kumar, S., Zhang, M., Stephanie, H.,: "Mode-selective Image Upconversion", 44, 98–101 (2018)
Labroille, G., Bertrand Denolle, P., Jian, P.G., Treps, N., Morizur, J.-F.: Efficient and mode selective spatial mode multiplexer based on multi-plane light conversion. Opt. Express **22**, 15599–15607 (2014)
Labroille, G., Bertrand Denolle, P., Jian, P.G., Treps, N., Morizur, J.-F.: Efficient and mode selective spatial mode multiplexer based on multi-plane light conversion. Opt. Express **22**, 15599–15607 (2014)
Liangjun, L., Zhao, S., Zhou, L., Li, D., Li, Z., Wang, M., Li, X., Chen, J.: 16 × 16 non-blocking silicon optical switch based on electro-optic Mach-Zehnder interferometers. Opt. Express **24**, 9295–9307 (2016)
Linh, H.D.T., Dung, T.C., Tanizawa, K., Thang, D.D., Hung, N.T.: Arbitrary arbitrary TE0/TE1/TE2/TE3 mode converter using 1×4 Y-junction and 4×4 MMI couplers. IEEE J. Sel. Top. Quantum Electron. **26**(2), 1–8 (2020)
Liu, M., Tang, M., Cao, M., Mi, Y., Guan, P., Ren, W., Ren, G.: All-fiber mode selective comb filter based on Mach-Zehnder interferometer. Optics Communications **492**, 1–5 (2021)
Liu, T., Yan, X., Liu, S., Sun, X., Zhang, D.: Ge2Sb2Se4Te1-assisted non-volatile silicon mode selective switch. Opt. Mater. Express **12**, 2584–2593 (2022)
Luo, L.-W., Ophir, N., Chen, C.P., Gabrielli, L.H., Poitras, C.B., Bergmen, K., Lipson, M.: WDM-compatible mode-division multiplexing on a silicon chip. Nat. Commun. **5**, 3069–3076 (2014)
Mojaver, K.R., Safaee, S.M.R., Morrison, S.S., Liboiron-Ladouceur, O.: Recent advancements in mode division multiplexing for communication and computation in silicon photonics. J. Lightwave Technol. **42**, 7860–7872 (2024)
Mulugeta, Tadesse, Rasras, Mahmoud: Silicon hybrid (de)multiplexer enabling simultaneous mode and wavelength division multiplexing. Optics Express **23**(2), 943–949 (2015)
Nguyen, V.H., Kim, I.K., Seok, T.J.: Silicon photonic mode-division reconfigurable optical add/drop multiplexers with mode-selective integrated MEMS switches. Photonics **7**, 80–90 (2020)
Paniccia, M.J.: A perfect marriage: optics and silicon. Optik Photonik **6**(2), 34–38 (2011)
Priti, R.B., Liboiron-Ladouceur, O.: Reconfigurable and scalable multimode silicon photonics switch for energy-efficient mode-division-multiplexing systems. J. Lightwave Technol. **37**(15), 3851–3860 (2019)
Priti, R., Pishvai Bazargani, H., Xiong, Y., Liboiron-Ladouceur, O.: Mode selecting switch using multimode interference for on-chip optical interconnects. Opt. Lett. **42**, 4131–4134 (2017)
Qiu, H., Yu, H., Hu, T., Jiang, G., Shao, H., Yu, P., Yang, J., Jiang, X.: Silicon mode multi/demultiplexer based on multimode grating-assisted couplers. Opt. Express **21**(15), 17904–17911 (2013)
Sharma, NeerajK.: Review of recent shared memory based ATM switches. Comput. Commun. **22**(4), 297–316 (1999)
Shen, W., Du, J., Xu, K., He, Z.: On-chip selective dual-mode switch for 2-μm wavelength high-speed optical interconnection. IEEE Photonics Technol. Lett. **33**(10), 483–486 (2021)
Soldano, M.P.B.: Optical multi-mode interference devices based on self-imaging: principles and applications. J. Light. Technol. **13**(4), 615–627 (1995)
Sun, S., Qidong, Y., Che, Y., Lian, T., Xie, Y., Zhang, D., Wang, X.: Mode-insensitive and mode-selective optical switch based on asymmetric Y-junctions and MMI couplers. Photon. Res. **12**, 423–430 (2024)
Tang, R.: Tanemura, T., Nakano, Y.: integrated reconfigurable unitary optical mode converter using MMI couplers. IEEE Photonics Technol. Lett. **29**(12), 971–974 (2017)
Tianhang Lian, M., Zhu, S.S., Sun, X., Che, Y., Lin, B., Wang, X., Zhang, D.: Mode-selective modulator and switch based on graphene-polymer hybrid waveguides. Opt. Express **30**, 23746–23755 (2022)
Wang, S., Hao, W.: "Monolithically integrated reconfigurable add-drop multiplexer for mode-division-multiplexing systems,''. Opt. Lett. **41**, 5298–5301 (2016)
Wang, J., He, S., Dai, D.: On-chip silicon 8-channel hybrid (de)multiplexer enabling simultaneous mode- and polarization-division- multiplexing. Laser Photonics Rev. **8**(2), L18–L22 (2014)
Wang, S., Feng, X., Gao, S., Shi, Y., Dai, T., Hui, Y., Tsang, H.-K., Dai, D.: On-chip reconfigurable optical add-drop multiplexer for hybrid wavelength/mode-division-multiplexing systems. Opt. Lett. **42**, 2802–2805 (2017)
Xiong, Y., Priti, R., Liboiron-Ladouceur, O.: High-speed two-mode switch for mode-division multiplexing optical networks. Optica **4**, 1098–1102 (2017)
Yong Zhang, Y., He, Q.Z., Qiu, C., Yikai, S.: On-chip silicon photonic 2×2 mode- and polarization-selective switch with low inter-modal crosstalk. Photon. Res. **5**, 521–526 (2017)

Zhang, M., Chen, K., Jin, W., Jieyun, W., Chiang, K.S.: "Electro-optic mode-selective switch based on cascaded three-dimensional lithium-niobate waveguide directional couplers,''. Opt. Express **28**, 35506–35517 (2020)
Zhao, N., Li, X., Li, G., Kahn, J.M.: Capacity limits of spatially multiplexed free-space communication. Nature Photon. **9**(12), 822–826 (2015)
Zi, X., Wang, L., Chen, K., Chiang, K.S.: Mode-selective switch based on thermo-optic asymmetric directional coupler. IEEE Photonics Technol. Lett. **30**(7), 618–621 (2018)